Journal of Marine Science and Application (2024) 23: 743-761
https://doi.org/10.1007/s11804-024-00519-x

RESEARCH ARTICLE

Hydrodynamic Analysis of Different Shapes of Moored Hybrid Floating Breakwater

Ranti Dev Vishwakarma[1] and Debabrata Karmakar[1]

Received: 04 April 2024 / Accepted: 20 September 2024

Abstract

The present study investigates the effect of moorings on hybrid floating breakwaters of different configurations based on potential flow theory. The mooring analysis is performed for the regular wave incidence for five different shapes of hybrid floating breakwaters, namely, rectangular, box, H, Π, and trapezoidal, integrated with a single J-shaped oscillating water column (OWC). The mooring lines are considered to be non-linear catenary sections that are analysed for open mooring and cross mooring configuration. The hydrodynamic analysis is performed using Ansys-AQWA and the effectiveness of the moorings is evaluated in terms of the mooring line tension and the floating structure's motion response, and comparisons are made for the influence of different mooring configurations and the implications of changing the design of the hybrid floating breakwater. The regular gravity wave frequency range is taken into consideration and the hydrodynamic properties are reported for the entire range of regular wave frequencies. Additionally, for a few chosen wave frequencies the analysis of structural forces and moment is performed for long and short waves. The study suggests that a hydrodynamically stable hybrid floating structure integrated with an oscillating water column can provide good and effective wave energy conversion and wave attenuation. Thus, with the help of the findings of the present study, the researchers will be able to examine the stability of hybrid floating breakwater structures under the action of regular waves with normal incidence.

Keywords Hybrid floating breakwater; Mooring analysis; Mooring configurations; Ansys-AQWA; Catenary mooring

1 Introduction

The protection to coast and marine structures from severe ocean waves is effectively provided by bottom fixed breakwater, but due to massive construction cost and material requirement along with interference with ocean current flows and sediment transport on sea bed, the moored floating breakwater is considered as viable alternative (Wang and Tay, 2011). The floating breakwaters are economical in the terms of construction and maintenance cost in comparison to bottom mounted breakwaters in deep waters and the floating breakwaters are having rapid construction, easy transportation and easy demolition which adds to its implementation perks (Dai et al., 2018). The floating breakwater with wave energy conversion capable hybrid systems can be categorized in four types which includes floating wave energy converter (WEC) arrays with harbour sheltering functions, floating breakwater integrated with oscillating buoy-type WEC systems, floating breakwater with oscillating water column type WEC systems, and floating breakwater with overtopping type WEC systems (Zhao et al., 2019). The studies performed by researchers suggest that a floating hybrid system is having a good frequency bandwidth in which the wave energy conversion and wave attenuation performance are efficient. The extensive review of the hybrid floating breakwaters of different types is performed and it is found to have benefits in terms of cost savings for building, installing, and maintaining structures,

Article Highlights

- The hydrodynamic performance of different configurations of moored hybrid floating breakwater is analysed considering J-shaped OWC.
- The effectiveness of the mooring and the implications of changing the design of the hybrid floating breakwater is performed to understand the novelty of the hybrid device.
- The mooring line tension in the seaside cable in the case of open mooring is noted to exceed the maximum expected tension as compared to cross mooring configuration.
- The box-shape hybrid floating breakwater (HFB) experiences highest structural forces and moment compared to different shapes of HFBs in both mooring configurations for long waves but for short waves the horizontal force is highest for Π-shaped HFB in open mooring configuration and H-shaped HFB in cross mooring configuration.

✉ Debabrata Karmakar
dkarmakar@nitk.edu.in

[1] Department of Water Resources and Ocean Engineering, National Institute of Technology Karnataka, Surathkal, Mangalore–575025, India

as well as the ability to harvest energy and safeguard coastlines from environmental harm simultaneously (Mustapa et al., 2017; Zhao et al., 2019). The mooring system performance is mainly governed by the factors such as motion response of the floating structure, mooring line tension, and anchor holding capacity (Yuan et al., 2014). The ongoing development of floating structures is significantly aided by numerical modelling, which gives developers the opportunity to explore a wide range of designs before investing (Pols et al., 2021).

Significant studies were performed in past few decades on the mooring dynamics of the floating breakwater. The two-dimensional numerical study for dynamics of floating body moored using elastic mooring lines found that a floating breakwater having small draft can attenuate wave more efficiently if proper mooring configuration implied (Yamamoto et al., 1980). In continuation, Yamamoto (1981) performed response analysis of moored floating breakwater in regular and irregular waves and concluded that an elastically moored floating breakwater response to random waves is similar to response to regular waves. Among various types of floating breakwaters, the studies on dual pontoon floating breakwater moored with linear elastic mooring lines observed that the floating structure's wave reflection characteristics heavily depend on its draft, spacing between pontoons, and stiffness of the mooring lines (Williams and Abul-Azm, 1997; Williams et al., 2000). Further, a detailed theoretical and experimental investigation of motion responses and mooring forces on floating pontoon breakwater revealed that the motion response with and without mooring are almost similar except for the resonance condition and the mooring arrangements had a significant impact on the mooring forces (Sannasiraj et al., 1998). The element free Galerkin's method to assess the hydrodynamic performance of a moored rectangular floating breakwater under the action of regular waves found that the solution accuracy of the method depends on size of domain and intermodal spacing. The study also observed quantifiable difference between slack and taut mooring cable forces (Lee and Cho, 2003). Similar performance study by Loukogeorgaki and Angelides (2005) revealed that there is increase in stiffness of the mooring cables as mooring configuration changed from slack to taut resulting in intense alteration of the floating breakwater's dynamic behaviour, ultimately improving floating breakwater effectiveness in wave attenuation. An experimental investigation on floating breakwater to assess wave transmission found that the lying length of the mooring rope on the ocean floor is significant for the effectiveness of floating breakwater as less lying length found to be improving the wave attenuation due to reduction in motion with short cable (Dong et al., 2008).

To overcome the limitations of the studies focused in unbounded domain, Elchahal et al. (2009) performed parametric and motion analysis of a moored floating breakwater of rectangular shape in a fluid domain of finite length with a vertical wall on leeside. The influence of the change in side wall clearance, draft, width, angle of inclination of mooring lines and mooring stiffness is performed on the floating breakwater performance. The study noted that, 30° angle of mooring line inclination to the floating structure is economically optimum and increasing the mooring line stiffness which resulted in improved stability of the floating breakwater ultimately reducing transmission of waves. The investigation on the connection between the multiple floating breakwater models moored with cables and connected with hinges is addressed by Diamantoulaki and Angelides (2011). The study concluded that the array's response depends strongly on number of hinge joints and number of mooring lines. A 3D experimental investigation on multiple box-type floating breakwater array connected using flexible connectors and moored using mooring chains is performed by Loukogeorgaki et al. (2014) for analysing the hydrodynamic performance under the action of normal and oblique regular waves and irregular waves. The reduction in wave period is noted for all oblique waves, which results in the reduction in the axial and shear forces on the connections as well as the tension in the mooring line. The study also revealed that, for 45° angle of incidence, the floating system is most efficient in terms of its functional and structural integrity. The laboratory experiment on a perforated floating breakwater with mooring found that the vortex created by the perforated floating breakwater significantly reduced the maximum tensions of various mooring systems (Yoon et al., 2018). Further, the experimental study on wave attenuation performance of the trapezoidal floating breakwater noted that force in mooring line and transmission of wave through trapezoidal floating breakwater, with bottom side wider than top side, is less than that in the case of rectangular floating breakwater (Nikpour et al., 2019). Apart from surface piercing floating breakwater, the recent studies in submerged floating breakwater by Liu and Wang (2020) considered different cross-sectional shapes of the breakwaters moored to the seabed. The study noted that there is a strong relation between motion, wave attenuation, and mooring tension with the motion of submerged body. A thorough study performed by Xu et al. (2019), on WECs and the mooring systems design revealed that the mooring system should not provide negative impact on the WEC's performance by lowering motion responses. The study on the quasi-static response of a moored floating body using catenary mooring towards minimizing the mechanical energy of the whole system is conducted by Li et al. (2021). The study found that the method proposed to predict the mooring response is approximately same as the simulation performed using Ansys-AQWA. Depalo et al. (2021) investigated the effect of mooring cable material, size, and pre-tension changes on WEC response under different mooring configurations.

The study noted that, unlike rigid lines, synthetic materials such as fibre ropes have highly nonlinear load-elongation characteristics, necessitating the use of a coupled dynamic time-domain analysis to analyse such nonlinear behaviours.

Recently, the experimental study by Liang et al. (2022) on the hydrodynamic performance of floating box-type breakwater with different mooring configurations reveals that the floating breakwater performs very efficiently for wave attenuation in fixed condition than that under mooring condition. The study also found that the mooring lines with less fairlaid length are effective for dissipation of long period waves. The study of submerged floating breakwater design by Zanden et al. (2022) suggest that wave attenuation is dominated by diffraction and radiation, as well as the new design is less effective in terms of attenuation as compared to box-type breakwaters. In order to improve the wave dissipation effect and the breakwater's resistance to harsh sea conditions, the hydrodynamic examination of the barge-type breakwater under crossed tilt mooring and front and rear direct pull mooring recommended employing the crossed tilt mooring method during construction (Cheng et al., 2023). The study noted that in the chain without a section resting on the seabed, the anchor chain forces and wave dissipation effect are noticeably better. The finding of the study by Zhao et al. (2023) regarding the dynamics of a multi-float hinge WEC with a nonlinear mooring system emphasise the importance of choosing appropriate mooring cables and modify their properties to maximise the performance of the WEC. Zhang et al. (2023) discussed the effect of cavitation for rigid and free surface boundaries to analyse the functionality and stability of any structure due to negative pressure induced in the bubble. According to a study of the hydrodynamic parameters of a multi-cylinder floating breakwater (Zang et al., 2024), the maximum mooring force of the floating breakwater increases with wind speed, current velocity, incidence wave height and period, and water depth. A study of a floating-point absorber with a catenary mooring system concluded that the mooring design is critical for station keeping, efficient power collection, and financial considerations of the WEC, and that the catenary mooring can provide steady support for the WEC to maintain its stable operating condition in Computational Fluid Dynamics (CFD) simulation (Zhang et al., 2024).

The studies performed by the researchers suggest that, the effectiveness of a floating breakwater in terms of its hydrodynamic performance can be enhanced by selecting proper mooring system and the same is applicable for the hybrid floating breakwaters. The present study deals with numerical analysis of moored hybrid floating breakwaters based on potential flow theory. The mooring performance for different mooring configuration with different shapes of hybrid floating breakwaters, for non-linear catenary mooring, is obtained in the present study. As studies performed by various researchers (Yamamoto, 1981; Sannasiraj et al., 1998; Li et al., 2021; Liang et al., 2022) have investigated two mooring configurations, namely, open mooring and cross mooring but the influence of the shape of the floating body has not been investigated, and the studies performed is having restrictions in motion. Thus, the present study examines the open and cross mooring configurations with different shapes of hybrid floating breakwater without any restriction on their motion. The five different cross-sections of hybrid floating breakwaters are integrated with oscillating water column wave energy converter and the cross-sections are chosen randomly considering similarities with rectangular cross-section which is the most studied floating breakwater shape. Moreover, the motion response analysis of the hybrid floating breakwater structures in different mooring cases are performed using Ansys-AQWA and included in the study.

2 Methodology and formulations

The Ansys-AQWA solver works on the principle of potential flow theory, which solves incident velocity potential φ_I, diffracted velocity potential φ_D and radiated velocity potential φ_R, and determine various hydrodynamic parameters related to motion response and mooring line response. According to potential flow theory, the region of fluid motion adjacent to a floating structure at a point in space $\vec{X}$ and time t can be represented as

$$\Phi(\vec{X}, t) = a_{\text{wave}}\left[\varphi_I + \varphi_D + \sum_{j=1}^{6}\varphi_{Rj}x_j\right]\mathrm{e}^{-\mathrm{i}\omega t} \tag{1}$$

where a_{wave} is the incident wave amplitude and x_j is the jth motion per unit wave amplitude.

2.1 Wave forces and equation of motion

The linearized Bernoulli's equation is used to determine the hydraulic pressure distribution when the potentials are known and from the pressure distribution various fluid forces are derived which can be categorized in two components namely, active and reactive. The active force $F_{a,j}$ is wave excitation force which is represented in jth direction by

$$F_{a,j} = F_{\text{FK},j} + F_{D,j} = -\int_S \mathrm{i}\omega\rho\varphi_I\hat{n}_j\,\mathrm{d}S - \int_S \mathrm{i}\omega\rho\varphi_D\hat{n}_j\,\mathrm{d}S \tag{2}$$

where $F_{\text{FK},j}$ is Froude-Krylov force in jth direction, $F_{D,j}$ is diffraction force in jth direction, $\hat{n}_j$ is generalised surface normal for jth direction, and S is wetted surface of the floating structure. The reactive force is radiation force $F_{r,ji}$ generated by the movement of the floating structure is generated due to ith motion in jth direction given by

$$F_{r,ji} = \int_S \omega\rho x_i \varphi_{R,i}^{\mathrm{Img}} \hat{n}_j \mathrm{d}S - \int_S \mathrm{i}\omega\rho x_i \varphi_{R,i}^{\mathrm{Re}} \hat{n}_j \mathrm{d}S \tag{3}$$

$$\text{or } F_{r,ji} = -A_{ji}\ddot{x}_i - B_{ji}\dot{x}_i \tag{4}$$

where A_{ji} is the added mass coefficient and B_{ji} is the wave radiation damping coefficient which can be represented as

$$A_{ji} = \rho\omega^{-1}\int_S \varphi_{R,i}^{\mathrm{Img}} \hat{n}_j \mathrm{d}S \tag{5}$$

$$B_{ji} = \rho\int_S \varphi_{R,i}^{\mathrm{Re}} \hat{n}_j \mathrm{d}S \tag{6}$$

In time-domain analysis, the radiation force time history is based on added mass, radiation damping and the actual motion response of the structure instead of response amplitude operators (RAOs). On using convolution method, the motion response equation takes the form given by

$$\{\boldsymbol{m} + \boldsymbol{A}_\infty\}\ddot{X}(t) + \boldsymbol{c}\dot{X}(t) + \boldsymbol{K}X(t) + \int_0^t \boldsymbol{R}(t-\tau)\dot{X}(\tau)\mathrm{d}\tau = \boldsymbol{F}(t) \tag{7}$$

where the mass matrix of structure is represented by $\boldsymbol{m}$, the added mass matrix at infinite frequency is represented by $\boldsymbol{A}_\infty$, the damping matrix excluding linear damping effect due to diffracting panels is represented by $\boldsymbol{c}$, the total stiffness matrix is represented by $\boldsymbol{K}$, and the velocity impulse function matrix is represented by $\boldsymbol{R}(t)$.

The response relation as in Eq. (7) can be written in terms of acceleration impulse function matrix $h'(t)$ given by

$$\{\boldsymbol{m} + \boldsymbol{A}_\infty\}\ddot{X}(t) + \boldsymbol{c}\dot{X}(t) + \boldsymbol{K}X(t) + \int_0^t h'(t-\tau)\dot{X}(\tau)\mathrm{d}\tau = \boldsymbol{F}(t) \tag{8}$$

where $h'(t) = \frac{2}{\pi}\int_0^\infty \frac{B(\omega)\sin(\omega t)}{\omega}\mathrm{d}\omega = \frac{2}{\pi}\int_0^\infty \{A(\omega) - \boldsymbol{A}_\infty\}\cos(\omega t)\mathrm{d}\omega$, $\boldsymbol{A}_\omega$ and $\boldsymbol{B}_\omega$ are added mass and damping matrix respectively. The Wheeler stretching method is adopted for accurate determination of dynamic or kinematic properties of particles of fluid below free wave surface, in ANSYS (2021) time domain solver. After application of the Wheeler stretching method the linear regular wave properties, such as, fluid particle velocity $\boldsymbol{V}$ and acceleration $\boldsymbol{a}$, free surface elevation ζ, and hydrodynamic pressure $p_t(t)$, at a location (X, Y, Z_0) below instantaneous incident wave surface is given by

$$\mathrm{Re}\{\boldsymbol{V}\} = \frac{\omega a_{\mathrm{wave}}\cosh k(Z+h)}{\sinh kh}\{\cos\psi, 0, \sin\psi\tanh k(Z+h)\} \tag{9}$$

$$\mathrm{Re}\{\boldsymbol{a}\} = \frac{\omega^2 a_{\mathrm{wave}}\cosh k(Z+h)}{\sinh kh}\{\sin\psi, 0, -\cos\psi\tanh k(Z+h)\} \tag{10}$$

$$\mathrm{Re}\{\zeta\} = a_{\mathrm{wave}}\sin\psi \tag{11}$$

$$p_t(t) = \frac{\rho g a_{\mathrm{wave}}\cosh k(Z+h)}{\cosh kh}\cos\psi - \rho g Z_0 \tag{12}$$

where $\psi = kX - \omega t + \alpha$, and α is wave phase.

2.2 Catenary mooring line forces

The mooring lines is significant in contributing to a structure's exterior forces and stiffness matrix which result is the static equilibrium condition and has impact on stability. The mooring line considered in the study is non-linear catenary mooring cable. The term non-linear generally implies that the stiffness or tension profile of the mooring cable varies along its length. The tension, stiffness, and profile of a catenary mooring line are determined by its immersed weight, length, and connection positions. The summary of the solution of catenary equation (ANSYS, 2021) is presented here and the detailed solution can be referred in Barltrop (1998).

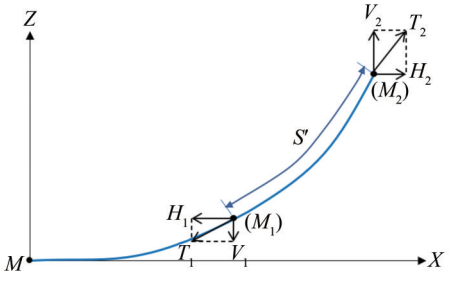

Figure 1 Profile of a catenary cable

The profile of the catenary cable (Figure 1) originating from point $M = (X, Y, Z)$ where slope is zero and, on its extension, the segment of points $M_1 = (X_1, Z_1)$ and $M_2 = (X_2, Z_2)$ is represented for which the horizontal vertical component of the tension equations is derived as

$$H_2 = H = \mathrm{AE}\left[\sqrt{\left(\frac{T_2}{\mathrm{AE}} + 1\right)^2 - \frac{2wZ_2}{\mathrm{AE}}} - 1\right] \tag{13}$$

$$X_2 = \frac{H_2}{w}\sinh^{-1}\left(\frac{wL_{\mathrm{us}}}{H_2}\right) + \left(\frac{H_2 L_{\mathrm{us}}}{\mathrm{AE}}\right) \tag{14}$$

$$V_2 = wL \text{ and } T_2 = \sqrt{H_2^2 + V_2^2} \tag{15}$$

where L_{us} represents unstretched length of catenary line

from M to M_2 for a tension force of T_2 at M_2, w represents the submerged weight per unit length, H_2 and V_2 represent the horizontal and vertical component of tension force respectively and AE is the stiffness per unit length. Considering a segment of unstretched length S' which is less than L_{us}, the position M_1 at the left end of segment is given by

$$X_1 = \frac{H}{w}\ln\left(\frac{V_2 + T_2}{V_1 + T_1}\right) + \frac{HS'}{\mathrm{AE}} \tag{16}$$

$$Z_1 = S'\left[\left(\frac{V_2 + V_1}{T_2 + T_1}\right) + \left(\frac{V_2 + V_1}{2\mathrm{AE}}\right)\right] \tag{17}$$

$$T_1 = \sqrt{\left(H_1^2 + V_1^2\right)} = \sqrt{\left(H^2 + \left(V_2 - wS'\right)^2\right)} \tag{18}$$

where H_1 and V_1 represents the horizontal and vertical force components for tension force T_1 respectively. The stiffness matrix $\boldsymbol{K}_g$ of each mooring line's which links centre-of-gravity displacements for the change in pressures and moments at the centre of gravity is given by

$$\boldsymbol{K}_g = \begin{bmatrix} I \\ R_a^{\mathrm{T}} \end{bmatrix} \boldsymbol{K} \begin{bmatrix} I & \boldsymbol{R}_a \end{bmatrix} + \begin{bmatrix} 0 & 0 \\ 0 & \boldsymbol{P}_m \boldsymbol{R}_a^{\mathrm{T}} \end{bmatrix} \tag{19}$$

where $\boldsymbol{R}_a = \begin{bmatrix} 0 & z & -y \\ -z & 0 & x \\ y & -x & 0 \end{bmatrix}$ and $\boldsymbol{P}_m = \begin{bmatrix} 0 & P_z & -P_y \\ -P_z & 0 & P_x \\ P_y & -P_x & 0 \end{bmatrix}$

x, y, z are coordinates of mooring attachment point on structure relative to centre of gravity, and P_x, P_y, P_z are the mooring line tension at attachment point in respective directions. On interaction with waves, the structure reacts and experience wave excitation force and produce translation and rotational motion. The motion of the floating structure create tension on the mooring lines if the floating structure is moored. Considering the dynamics of cables, the wave excitation force is ignored and the hydrodynamic force F_h acting on a cable element is given by

$$F_h = F_b + F_d - m_a\left[\boldsymbol{a}_j, \boldsymbol{a}_{j+1}\right]^{\mathrm{T}} \tag{20}$$

where F_b represents the buoyant force, F_d represents the drag force, m_a represents the added mass, and $\boldsymbol{a}_j$ represents the acceleration of cable at jth node. The drag force on the mooring line element is expressed in a simplified time-dependent form as

$$F_d(t) = -\frac{1}{4}C_x\rho_w D_j L_j \left|A_j\left\{\boldsymbol{U}_j(t) - \boldsymbol{V}_j(t)\right\}\right| A_j\left\{\boldsymbol{U}_j(t) - \boldsymbol{V}_j(t)\right\} - \frac{1}{4}C_d\rho_w D_j L_j \left|N_j\left\{\boldsymbol{U}_j(t) - \boldsymbol{V}_j(t)\right\}\right| N_j\left\{\boldsymbol{U}_j(t) - \boldsymbol{V}_j(t)\right\} \tag{21}$$

where $\boldsymbol{V}_j(t)$ and $\boldsymbol{U}_j(t)$ are the matrix form of the structural velocity and current velocity at jth node at time t respectively, C_d and C_x are the transverse and inline drag coefficients respectively, L_j and D_j are unstretched elemental length and diameter respectively, and A_j and N_j are axial and normal directional tensor respectively.

3 Numerical model description

The floating breakwaters (FB) of different shape integrated with oscillating water column (OWC), also named as hybrid floating breakwater (HFB), is considered in the present study are having same draft of HFB to water depth ratio d/h = 0.1 and width of HFB to water depth ratio b/h = 0.3, which is taken approximately similar to the study of Rajabi and Ghassemi (2021). For better comparison, HFBs have the same volume of displaced water for all study model shapes, and the length of HFB to water depth ratio L/h is not same for all study models to maintain the equal weight of models. The displaced water volume considered in this study is 360 m^3 for all shapes of HFB. The schematic representation for two different mooring configurations namely, open mooring (OM) and cross mooring (CM) are presented in the Figure 2 and Figure 3, respectively and the HFBs dimensions are given in Table 1.

The OWC is considered as J-type OWC and it is presented in Figure 4. The OWC dimensions are kept same in all shapes of FB and it is having equal chamber width c_x and inlet height c_i. The OWC length c_l equals to two times of chamber width, the air flow outlet diameter c_o to chamber width ratio is 0.5, chamber width to water depth ratio c_x/h equals to 0.05, and radius of the curved section of the geometry (R_1 and R_2) are fixed with respect to c_x as R_1/c_x= 1.0, and R_2/c_x = 2.0.

Table 1 Dimensions of different hybrid floating breakwater models

HFB type	FB dimensions						OWC dimensions		
	b/h	d/h	L/h	t/h	b_1/h	b_2/h	c_x/h	c_0/h	c_l/h
Box	0.30	0.10	0.67	0.05	-	-	0.05	0.025	0.10
H	0.30	0.10	0.67	0.05	-	-	0.05	0.025	0.10
Π	0.30	0.10	0.89	-	-	-	0.05	0.025	0.10
Rectangle	0.30	0.10	0.44	-	-	-	0.05	0.025	0.10
Trapezoidal	0.30	0.10	0.53	-	0.20	0.37	0.05	0.025	0.10

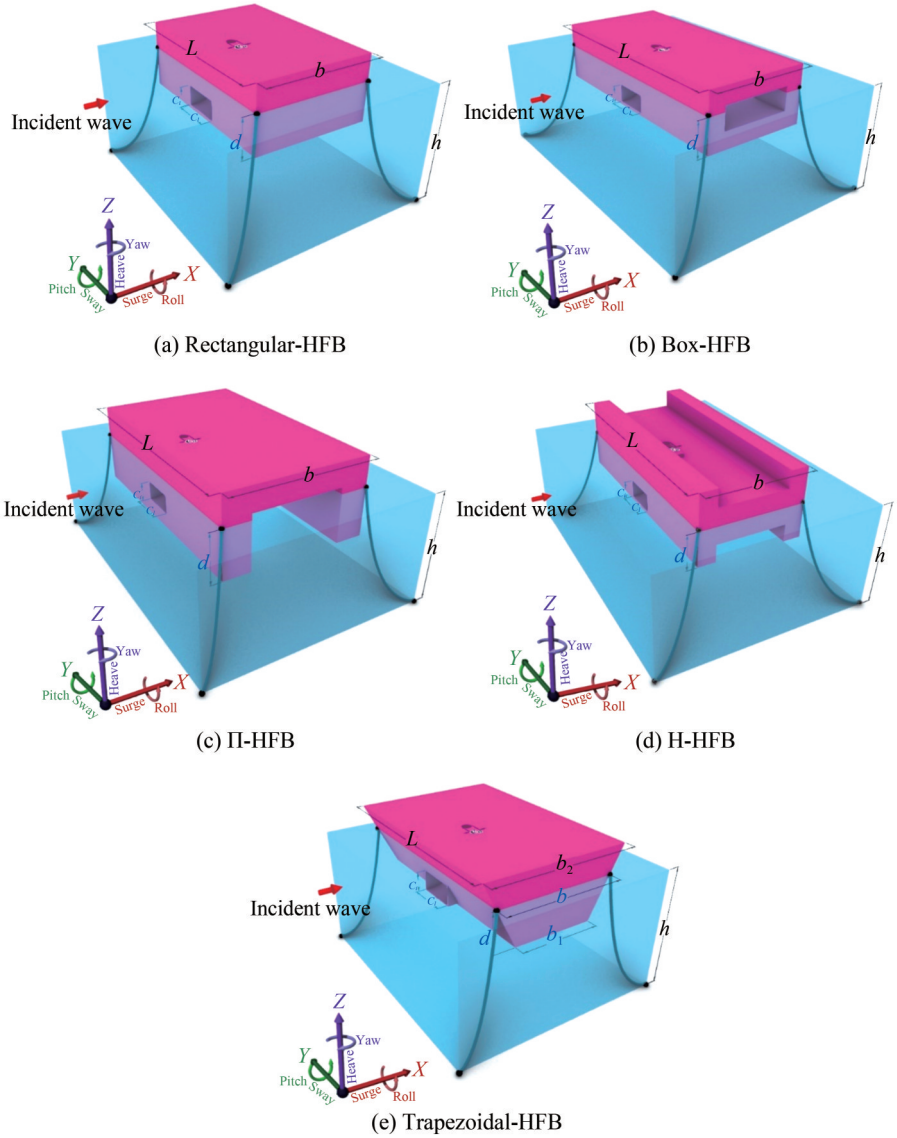

Figure 2 Three-dimensional schematic representation in open mooring configuration

The mooring line properties considered in this study are similar to the study performed by Li et al. (2021) on moored floating structure. The non-linear catenary section mooring line properties, and connection points on structure and seabed, are tabulated in Table 2 and Table 3 respectively. The mooring lines positions are kept at an angle 45° in both vertical and horizontal plane. The mooring line opted for the study is slacked catenary mooring line connected at two different levels of structure as per mooring configuration. In the case of open mooring, the mooring line is connected at sea water level and for cross mooring, the mooring line is connected at the base of the floating structure.

4 Numerical results and discussion

The performance of the mooring lines attached with hybrid floating breakwater structure is assessed using three-dimensional time response analysis in Ansys-AQWA. The mooring line strength is examined by determination of highest mooring tension $F_{T\max}$ experienced by the mooring lines in regular waves for different non-dimensional wave numbers ($0.1 \leqslant kh \leqslant 8.0$). Firstly, the validation of the numerical model in Ansys-AQWA is performed and then the models considered for the study are simulated. The whole cable tension experienced by the mooring lines is compared by changing the shape of moored floating structure namely, rectangular, box, Π, H and trapezoidal in different configurations of mooring. Additionally, motion response is obtained in surge, heave, and pitch motions for moored hybrid floating structures for mooring configuration with least mooring tension. Only surge, heave, and pitch motions are considered in the study due to its dominance among full six degrees of freedoms for regular wave with $\theta = 0°$.

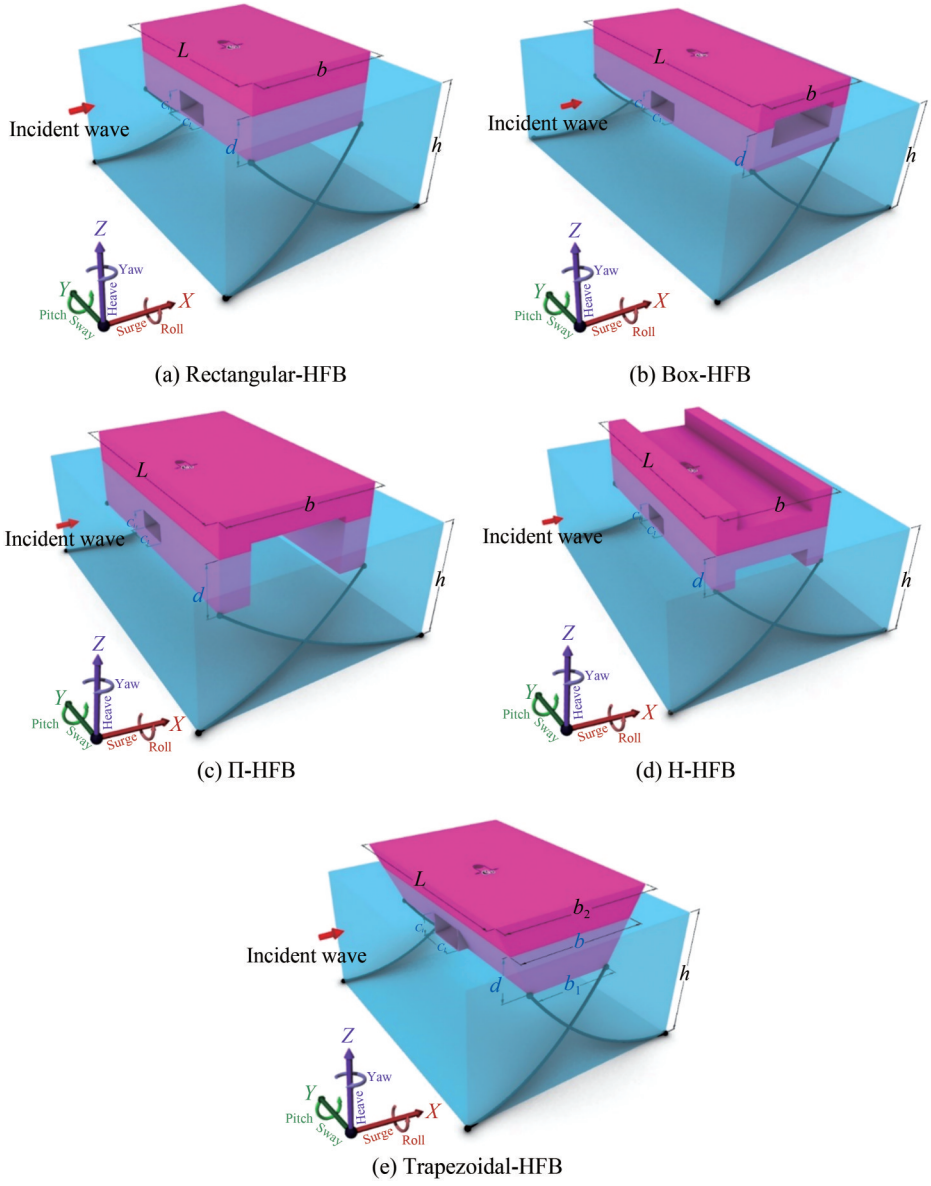

Figure 3 Three-dimensional schematic representation in cross mooring configuration

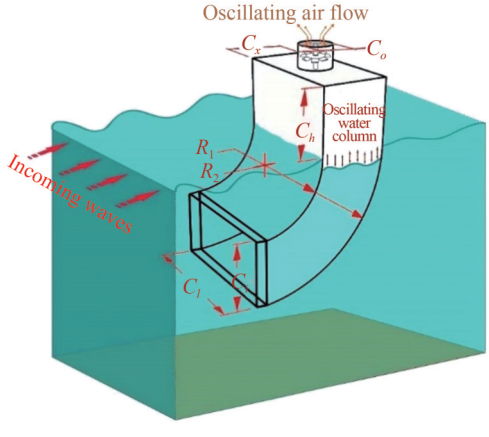

Figure 4 Schematic of J-type OWC model

Table 2 Non-linear catenary section mooring line parameters

Parameters	For open mooring	For cross mooring
Line diameter (m)	0.080 9	0.080 9
Unstretched length (m)	45	49
Cross-sectional area (m^2)	0.005 1	0.005 1
Line stiffness (N/m)	1.25×10^6	1.25×10^6
Maximum expected tension (N)	2.50×10^5	2.50×10^5

Table 3 Mooring line connection points coordinates

HFB Type	Connection points	For open mooring configuration	For cross mooring configuration
Rectangular	Fairlead points (*X*, *Y*, *Z*)	(−4.50, −12.83, 0.00); (−4.50, 12.83, 0.00); (4.50, 12.83, 0.00); (4.50, −12.83, 0.00)	(−4.00, −12.83, −3.00); (−4.00, 12.83, −3.00); (4.00, 12.83, −3.00); (4.00, −12.83, −3.00)
	Anchor points (*X*, *Y*, *Z*)	(−25.71, −34.05, −30.00); (−25.71, 34.05, −30.00); (25.71, 34.05, −30.00); (25.71, −34.05, −30.00)	
Box	Fairlead points (*X*, *Y*, *Z*)	(−4.50, −9.50, 0.00); (−4.50, 9.50, 0.00); (4.50, 9.50, 0.00); (4.50, −9.50, 0.00)	(−4.00, −9.50, −3.00); (−4.00, 9.50, −3.00); (4.00, 9.50, −3.00); (4.00, −9.50, −3.00)
	Anchor points (*X*, *Y*, *Z*)	(−25.71, −30.71, −30.00); (−25.71, 30.71, −30.00); (25.71, 30.71, −30.00); (25.71, −30.71, −30.00)	
Π	Fairlead points (*X*, *Y*, *Z*)	(−6.00, −9.50, 0.00); (−6.00, 9.50, 0.00); (6.00, 9.50, 0.00); (6.00, −9.50, 0.00)	(−5.50, −9.50, −4.00); (−5.50, 9.50, −4.00); (5.50, 9.50, −4.00); (5.50, −9.50, −4.00)
	Anchor points (*X*, *Y*, *Z*)	(−27.21, −30.71, −30.00); (−27.21, 30.71, −30.00); (27.21, 30.71, −30.00); (27.21, −30.71, −30.00)	
H	Fairlead points (*X*, *Y*, *Z*)	(−4.50, −9.50, 0.00); (−4.50, 9.50, 0.00); (4.50, 9.50, 0.00); (4.50, −9.50, 0.00)	(−4.00, −9.50, −3.00); (−4.00, 9.50, −3.00); (4.00, 9.50, −3.00); (4.00, −9.50, −3.00)
	Anchor points (*X*, *Y*, *Z*)	(−25.71, −30.71, −30.00); (−25.71, 30.71, −30.00); (25.71, 30.71, −30.00); (25.71, −30.71, −30.00)	
Trapezoidal	Fairlead points (*X*, *Y*, *Z*)	(−4.50, −7.50, 0.00); (−4.50, 7.50, 0.00); (4.50, 7.50, 0.00); (4.50, −7.50, 0.00)	(−2.50, −7.50, −3.00); (−2.50, 7.50, −3.00); (2.50, 7.50, −3.00); (2.50, −7.50, −3.00)
	Anchor points (*X*, *Y*, *Z*)	(−25.71, −28.71, −30.00); (−25.71, 28.71, −30.00); (25.71, 28.71, −30.00); (25.71, −28.71, −30.00)	

4.1 Validation of numerical model

The numerical method using time response analysis of Ansys-AQWA, is validated for mooring tension experienced by a catenary mooring attached with a rectangular floating breakwater model. The rectangular breakwater model considered by Diamantoulaki and Angelides (2011) is studied using the 3D hydrodynamic analysis code WAMIT.

The moored floating breakwater model is having the dimensions as b/h = 0.4, d/h = 0.077, and L/h = 2.0 along with catenary mooring of 0.033 m diameter with initial length of 30 m. The validation is performed for the maximum tension in front side mooring lines (Figure 5). The result obtained is compared for the range of wave frequencies presented in terms of breakwater width to wave length ratio within $0.1 \leqslant b/\lambda \leqslant 1.5$.

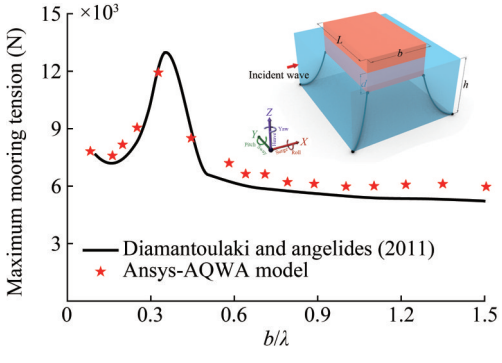

Figure 5 Validation of maximum mooring tension versus b/λ experience by catenary mooring

The validation for motion response is performed for a rectangular floating breakwater model in frequency domain using Ansys-AQWA for the study of Rajabi and Ghassemi (2021). The rectangular floating breakwater model is having b/h = 0.333, d/h = 0.067, and L/h = 0.667. The validation results are obtained for heave and pitch motion and plotted with respect to wave periods (Figure 6).

The determination of transmission coefficient based on diffraction theory using Ansys-AQWA is validated with the results of an experimental study by Ji et al. (2015) in Figure 7 for a rectangular floating breakwater with b/h = 0.50, d/h = 0.10, and L/h = 0.76 for normal wave direction.

The Figures 5-7, convincingly demonstrates that the mooring tension and response amplitude operators obtained using Ansys-AQWA model is almost similar to the results from Diamantoulaki and Angelides (2011), Rajabi and Ghassemi (2021), and Ji et al. (2015), respectively.

4.2 Mooring line performance

The performance of the mooring lines is assessed for different shapes of hybrid floating breakwater in different mooring configurations using hydrodynamic response analysis. The numerical analysis considers monochromatic linear waves with wave heading angle $\theta = 0°$ and wave amplitude equals to 0.5 m for dimensionless wave number ranging between $0.1 \leqslant kh \leqslant 8.0$. In order to maintain the accuracy of the results along with saving of the analysis time, the time step used for the simulations is 0.001 s for a

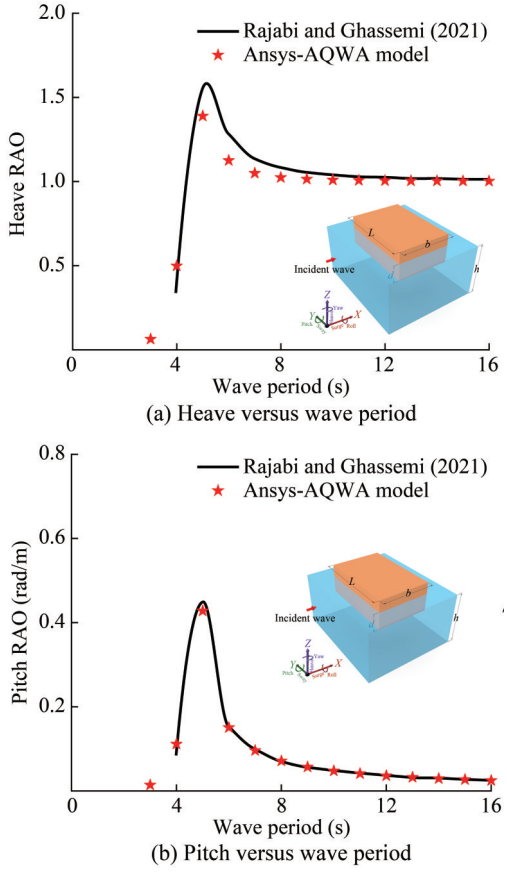

Figure 6 Validation of motion response (RAOs)

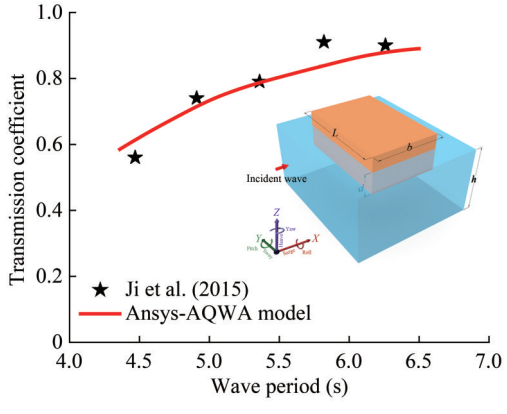

Figure 7 Validation of transmission coefficient versus wave period for rectangular floating breakwater

total response time of 100 s. Therefore, the $F_{T\max}$ presented here for a continuous regular wave incidence time of 100 s and time response plot are presented for $kh = 1.00$ and $kh = 4.18$ representing wave frequencies for intermediate water region and deep water region.

4.2.1 Effect of mooring configurations

The present study assesses the effect of mooring configurations in terms of the mooring line tension experienced by the mooring lines attached with HFBs in OM and CM configurations. The arrangement of mooring lines in which they are connected with the structure and the anchor points is important as it may improve the floating breakwater performance (Yamamoto et al., 1980; Sannasiraj et al., 1998). The $F_{T\max}$ experienced by different shape of HFBs in both configurations of mooring is discussed separately for each shape of the HFB.

In Figure 8, $F_{T\max}$ for both mooring configurations in the case of rectangular-shape HFB seemed to be confined within $50\,\text{kN} < F_{T\max} < 100\,\text{kN}$. The tension in mooring cable anchored to the sea side (SSC) is greater than tension mooring cable anchored to lee side (LSC) in deep water region ($kh > 3.14$) and in case of OM the difference in the tension in mooring cable is clearly visible. Continuous wave incidence causes the floating body to drift in the wave direction, causing extra tension to develop on the sea-side cable. On comparing the OM and CM configuration of mooring of rectangular-shape HFB, it is observed that $F_{T\max}$ in CM is about 3%–18% less than $F_{T\max}$ in OM for intermediate and deep-water region ($kh > 2.31$). The reason for less mooring tension experienced by mooring lines in CM configuration may be due to the transmission of wave across the structure without putting much stress on the floating body, which could result in less motion, causing mooring lines not to stretch beyond its slack. The similar phenomenon of high wave transmission is noted by Sannasiraj et al. (1998) in the case of CM is found for the rectangular floating breakwater.

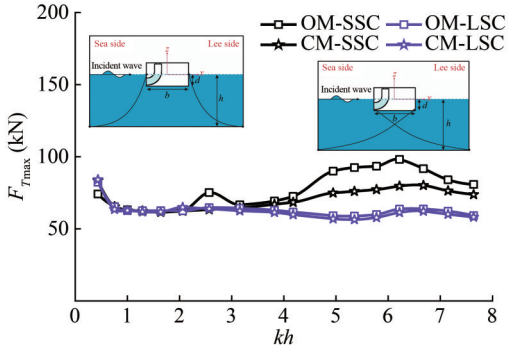

Figure 8 Maximum mooring tension versus kh for catenary moored rectangular-shape HFB considering $d/h = 0.1$, $b/h = 0.3$, and $\theta = 0°$

In the case of box-shape HFB (Figure 9), $F_{T\max}$ in both OM and CM configuration is confined within $60\,\text{kN} < F_{T\max} < 100\,\text{kN}$ for most of the range of non-dimensional wave number except $0.85 < kh \leqslant 1.0$. For $0.85 < kh \leqslant 1.0$, the highest mooring tension is observed in both mooring configurations. The excessively high value of mooring tension in the case of box-shape HFB within $0.87 \leqslant kh \leqslant 1.00$ is due to the resonant motion of the structure in the roll direction, as the natural frequency of the moored structure in roll motion is noted to be within the same range.

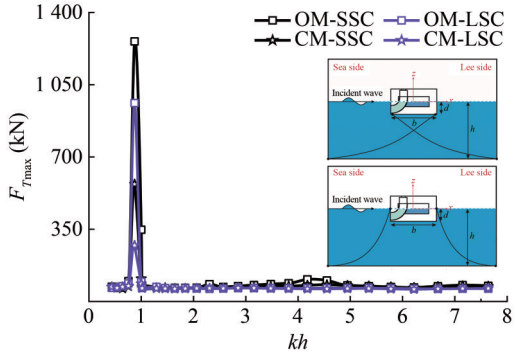

Figure 9 Maximum mooring tension versus kh for catenary moored box-shape HFB considering $d/h = 0.1$, $b/h = 0.3$, and $\theta = 0°$

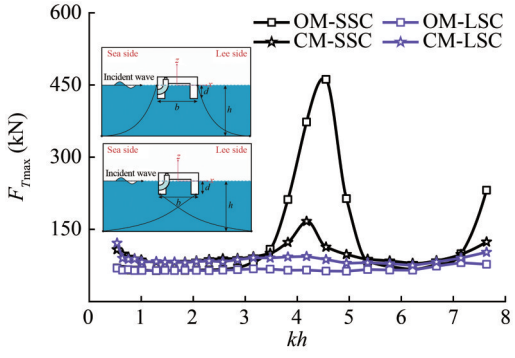

Figure 10 Maximum mooring tension versus kh for catenary moored Π-shape HFB considering $d/h = 0.1$, $b/h = 0.3$, and $\theta = 0°$

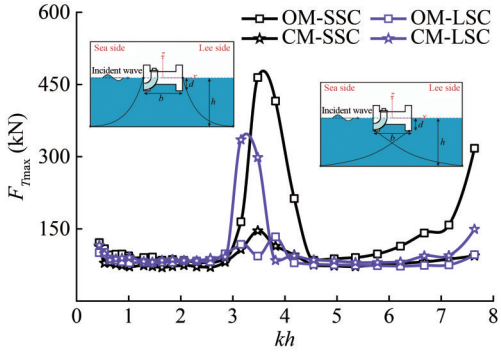

Figure 11 Maximum mooring tension versus kh for catenary moored H-shape HFB considering $d/h = 0.1$, $b/h = 0.3$, and $\theta = 0°$

Further, it is observed that the $F_{T\max}$ in CM is about 50%−70% less than $F_{T\max}$ in OM within $0.85 < kh \leqslant 1.0$. For the rest of the range of wavenumber the $F_{T\max}$ in CM is about 3%−27% less than $F_{T\max}$ in OM configuration. The highest value of the $F_{T\max} \simeq 1\,260$ kN which occurs in SSC of OM configuration for $kh = 0.87$. Among the analyzed wavenumbers, the $F_{T\max} \simeq 462$ kN in mooring line attached to Π-shape HFB (Figure 10) has its maximum value of mooring tension $F_{T\max}$ in OM configuration for SSC at $kh = 4.55$ which may be caused by excessive linear movement (towards the lee-side) or rotational movement (in anticlockwise direction) of the Π-shape HFB, causing stretch in sea side cable. The $F_{T\max}$ of SSC in CM configuration is about 15%−55% higher than the OM configuration for $0.30 < kh < 3.15$ and $5.35 < kh < 6.68$. Apart from earlier mentioned range of kh, the $F_{T\max}$ of SSC in CM configuration is about 40%−75% less than OM configuration. The large pitching motion within $3.5 < kh < 5.0$, generates tensile forces on sea-side cable in open mooring, but the same cable in cross mooring configuration is attached to the floating structures on the other end, which is towards the harbour region, and as the floating body rotates towards the harbour reason in pitching motion (in anticlockwise direction), causing the backend of the HFB to go below water line, which may create less tension on sea-side cable in the case of cross mooring compared to sea-side cable in the case of open mooring. Further, $F_{T\max}$ in LSC is having 11%−45% higher value in case of CM compared to OM for full range of considered wavenumber. The reason for high tension in LSC in case of CM may be due to the fact that as wave hits the floating body the dominant rotational motion causes the stretching of the mooring lines anchored to lee side (LSC) in case of CM.

Figure 11 shows $F_{T\max}$ for both mooring configurations, in the case of H-shape HFB, is below 150 kN for shallow and intermediate water region ($kh < 3.14$). This could be due to the larger incident wave length relative to the width of the floating structure model, resulting in waves passing through and minimal tension on mooring lines. In the case of full considered wave numbers, the $F_{T\max}$ for SSC in CM configuration is about 10%−30% lower than OM configuration and near peak values the same decrement is about 55%−73%. But in LSC the tension value in CM is about 5%–20% higher than OM and for near transition region of intermediate to deep water depth ($3.1 < kh < 3.5$) an 1.6–2.1 times increase in $F_{T\max}$ of LSC, with respect to tension in OM, is observed when CM is considered. This can be due to the high pitch motion in clockwise direction which causes the stretching of lee side mooring lines in CM same as the stretching of SSC in case of OM.

Considering the mooring tension for trapezoidal-shape HFB (Figure 12), it is clear that $F_{T\max}$ in CM for SSC is less than the $F_{T\max}$ in OM and the reduction is about 10%–25% for intermediate and shallow water region and little high reduction in deep water region of about 25%–73%. A possible cause for this decrease in mooring line tension in cross-mooring could be the positioning of the seaside mooring line with respect to the actual movement of the floating body. But the LSC less mooring tension reduction is noted of about 5%−15% when compared to OM. The minimum mooring tension of 61 kN in OM and 55 kN in CM is observed for full deep-water region which occurs because there is no significant stress on the mooring line on lee side apart from initial stresses due to its own weight and stiffness. For both configurations, the mooring line tension is confined within 55 kN $< F_{T\max} <$ 125 kN, which can be

due to limited motion response of the trapezoidal-shape HFB for the studied wavenumbers.

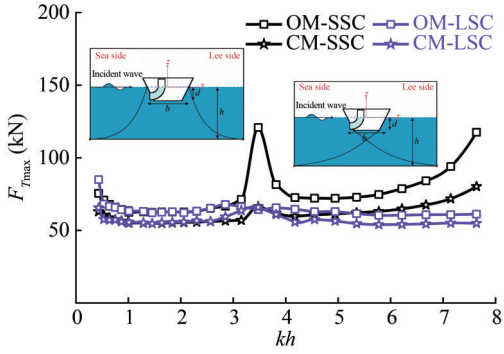

Figure 12 Maximum mooring tension versus kh for catenary moored trapezoidal-shape HFB considering $d/h = 0.1$, $b/h = 0.3$, and $\theta = 0°$

4.2.2 Effect of shape of HFBs

The shape of HFB can affect the performance of the floating structure and can result in the variation in mooring line tension with respect to different HFB. As discussed earlier in model description that all shapes of HFBs have approximately same volumetric displacement of water so that proper comparison on the basis of shape can be made. The $F_{T\max}$ variation is presented in Figure 13 while keeping a single mooring configuration and constant wave incidence angle of 0° for the regular wave. The study is important as it will help to deduce the performance of mooring line in different floating bodies because when the shape of the HFB changes, it results in change in diffraction properties of the body which results in different motion response for each shape leading to changes in mooring forces. The motion responses of different shapes are presented in Figure 13.

Figure 13(a) shows the variation of $F_{T\max}$ for the SSC in case of OM, and it can be observed that excessive mooring tension occurs for Π and H-shape HFB withing $3.45 \leqslant kh \leqslant 4.95$. The reason behind the excessive mooring tension for $3.45 \leqslant kh \leqslant 4.95$ may be due to the high rotational motion (i.e., pitch motion) of the H and Π-shape HFBs in the range of wave numbers, which is arrested by the mooring lines and it causes mooring line to stretch to its tensile capacity. Figure 13(b) represents the $F_{T\max}$ in LSC for OM and for each shape lee side mooring line in OM experiences less tension than SSC. The $F_{T\max}$ in CM for SSC and LSC (Figure 13(c), and Figure 13(d)), H-shape HFB shows different behaviour that other HFBs in terms of higher tension (about 5% to 25%) on LSC than that of SSC. But for $3.1 < kh < 3.5$ it shows 1.1–2.1 times increase in $F_{T\max}$ in LSC over SSC. The continuous propagation of waves of the same intensity on the H-shape HFB for an extended period of time causes the floating structure to drift towards the lee side; however, due to the mooring length limit, further

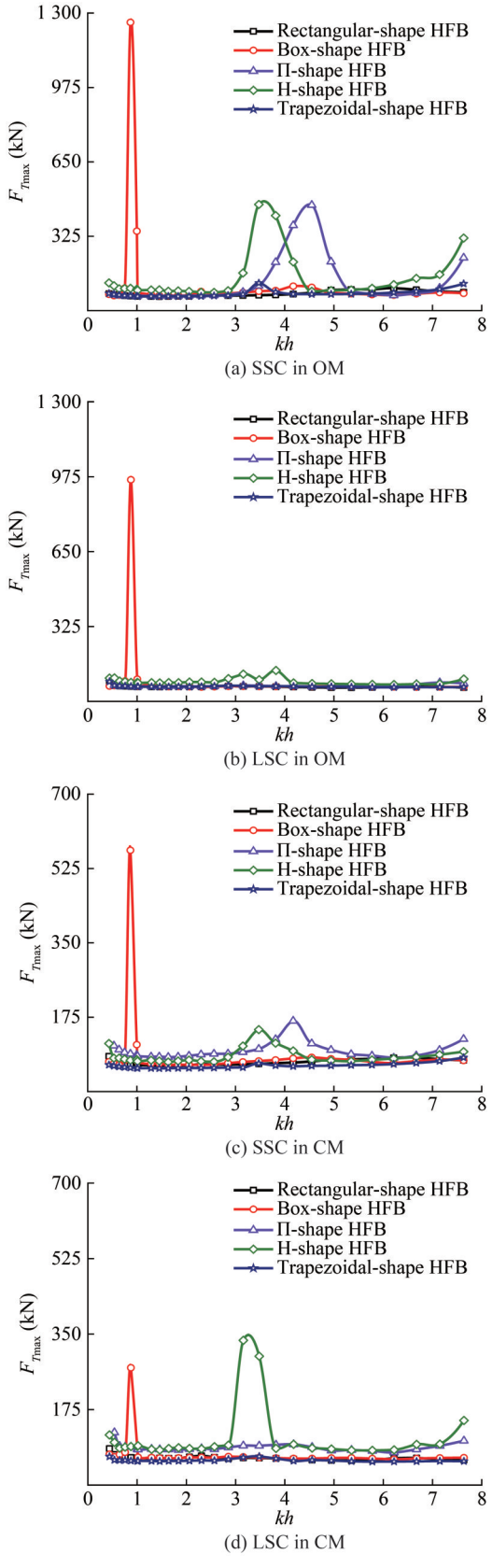

Figure 13 Comparison of mooring tension versus kh of different HFBs considering $d/h = 0.1$, $b/h = 0.3$, and $\theta = 0°$

drifting is restricted, and the restoring force resulting in the seaside cable tries to bring the structure to its original position. The rotation of the floating body causes the leeside cable in the CM configuration to virtually extend to a point where further tightening can increase cable tension. Therefore, these effects, in combination with the trough of the wave exsert tension on the structure, causing it to abruptly move in the direction opposite to incident wave, which may result in high tension in lee side mooring. Further, from Figure 13, it is observed that least mooring tension over the analysis wave number range is experienced by the mooring lines of the trapezoidal-shape HFB in CM configuration. The reason behind least experienced mooring tension by trapezoidal-shape HFB is due to least motion response among all shapes of HFBs for the considered wave number range. Further, the exceedance of mooring line tension beyond the value of maximum expected tension, for HFBs in some wave numbers (i.e., $0.87 \leqslant kh \leqslant 1.00$, $4.55 \leqslant kh \leqslant 4.95$, and $3.15 \leqslant kh \leqslant 3.82$ respectively for box, Π, and H-shape HFBs) can cause the mooring line failure in terms of snapping of mooring line if tension is way beyond the tolerance.

4.3 Motion response of moored HFBs

The motion response of a floating structure is key parameter in the investigation of mooring forces and wave attenuation due to floating breakwater. This is due to the fact that motion of the floating body will stretch the mooring lines if movement exceeds to greater extent from its equilibrium position (Liang et al., 2022). Due to the dominance of surge, heave, and pitch motion among all motions in six degrees of freedoms for normal wave incidence (i.e., $\theta = 0°$) for the study models of HFBs, the present section focuses on RAOs of the three motions. The RAOs for HFB with mooring is determined with the help of frequency domain analysis for the CM case, as most of the moored HFBs shows less mooring line tension in CM configuration and the RAOs of moored HFBs are compared with no mooring case. The stiffness due to attachment of mooring lines to the structures is added to the Ansys-AQWA model as an additional stiffness matrix to analyse the effect of mooring on structures hydrodynamic characteristics.

In Figure 14, it can be observed that for moored HFBs, the surge motion peaks diminishes and results in almost same surge motion for all models of HFBs. For $2.2 < kh < 4.2$, the high values of surge motion for H, Π, and trapezoidal shape HFBs is due to occurrence of pitch resonance in that region. In the case of with and without mooring motion amplitude in surge motion, the study shows that for most of the considered wave numbers, the surge RAO is approximately same for all shape of HFBs except for H, Π, and trapezoidal shape HFBs within $2.2 < kh < 4.2$. The addition stiffness applied to the floating structure due to the mooring lines is primary reason for elimination of excessive surge near pitch resonance for these shapes.

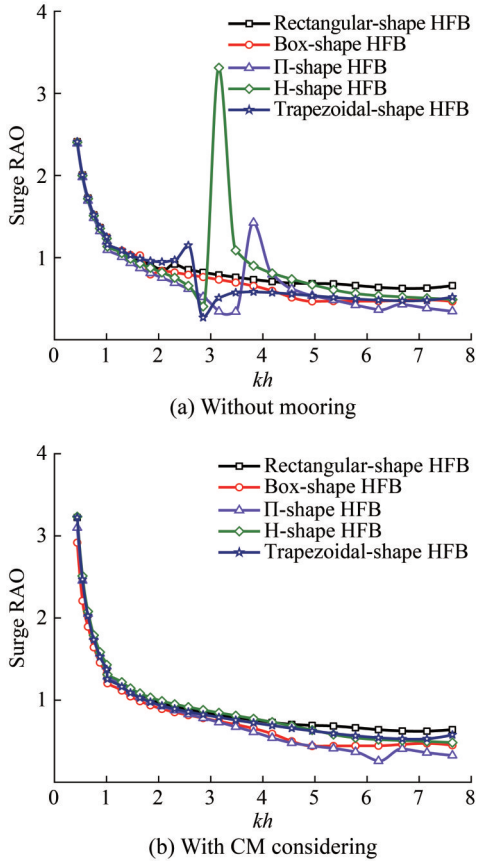

Figure 14 Surge RAO verses kh for different HFBs in case of $d/h = 0.1$, $b/h = 0.3$, and $\theta = 0°$

Figure 15 shows that the heave response of all HFBs in case of with and without mooring is almost same leading to no effect of mooring line on the heave motion as noted by Sannasiraj et al. (1998). Due to slacked mooring, there is no effect on heave motion for all shapes of HFBs. The same reason can be sought for no effect on surge motion for rectangular and box type HFBs and for other shapes $kh < 2.2$ and $kh > 4.2$. The heave RAO for all shapes in shallow and intermediate water region ($kh \leqslant 3.14$) is observed to be approximately same and near to 1 m/m. In the deep-water region ($kh > 3.14$) the heave motion starts picking up and peak values for all shapes is observed in this region. The reason for the heave motion approximately equal to 1 m/m may be due to the motion of the floating body in heave direction is same as wave amplitude for long waves (i.e., in shallow and intermediate water region). Among all HFB models the trapezoidal-shape HFB shows least and approximately uniform response over considered wave numbers, in surge and heave motion. This can be due to the inclined face towards the wave incident side causing hydrodynamic forces to operate indirectly rather than directly

on the floating structure, leading to a reduced motion response for the trapezoidal-shaped HFB.

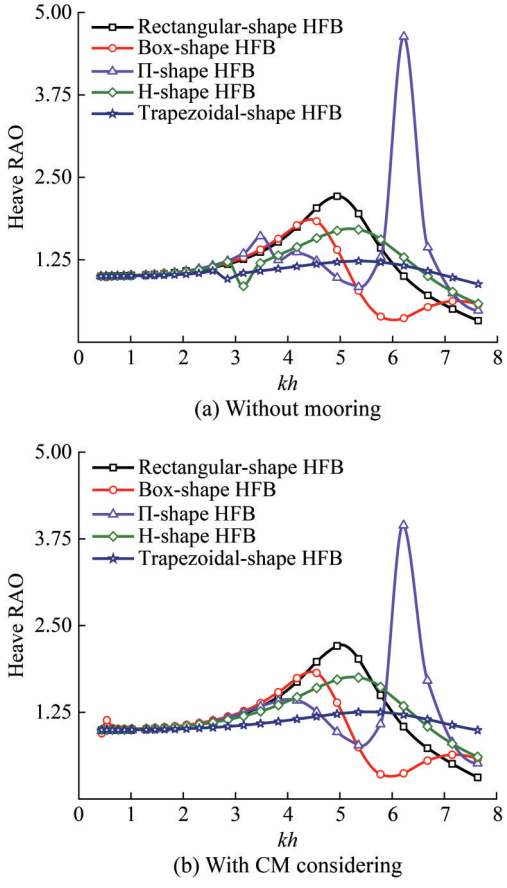

Figure 15 Heave RAO verses kh for different HFBs in case of $d/h = 0.1$, $b/h = 0.3$, and $\theta = 0°$

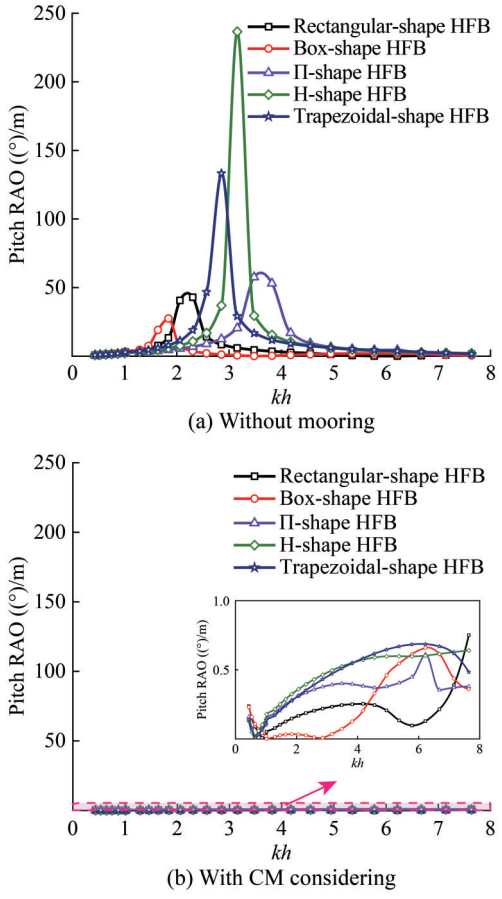

Figure 16 Pitch RAO verses kh for different HFBs in case of $d/h = 0.1$, $b/h = 0.3$, and $\theta = 0°$

In Figure 16, for all shapes of HFBs, it can be observed that when mooring lines are attached with HFBs their pitch motion is decreased by about 70%−99% and confined to the pitch RAO value below 1(°)/m. The gravitational force on the slacked catenary mooring line due to its own weight and additional hydrodynamic stiffness in rotational motions provided by mooring connection may be the reason for arrest of pitch motion. Further, it can be observed that the peak amplitude of pitch motion in case of HFBs without mooring (Figure 16(a)) lies within $1.8 < kh < 3.8$ and when HFBs are moored (Figure 16(b)) the same motion is having peak value for $kh > 6.0$. The exceptionally high value of pitching motion RAO in case of HFBs without mooring can be due to resonance phenomena caused by the proximity of the incident wave frequency with the structure's natural frequency.

4.4 Structural forces and moment

The investigation of forces and moments encountered on the floating structure due to the action of waves is required to be analysed in order to build a floating structure capable of resisting external forces. In addition to the mooring lines, the wave radiation and diffraction, linear damping, gravitational, and hydrostatic forces contribute to the total forces and moment experienced by the floating body. The change in the structural force and moment at the centre of gravity (CG) of the floating structure is analysed for regular incident wave having amplitude of 0.5 m and wave frequency corresponding to $kh = 1.00$ and $kh = 4.18$ respectively. The time history of total structural forces and moments is represented for different mooring configurations considering different HFB models. The forces and moments in surge, heave, and pitch directions are investigated in the present study due to the dominance of these three motions among the six degrees of freedom of motion. The horizontal force component F_x along x-direction, vertical force component F_z along z-direction and the moment component M_y in y-direction is analysed for HFBs of various shapes such as R-HFB for rectangular-shape, B-HFB for box-shape, Π-HFB for Π-shape, H-HFB for H-shape, and T-HFB for trapezoidal-shape.

Figure 17 shows the variation of F_x, F_z, and M_y at CG of different configurations of HFB models, moored in OM

configuration for regular incident wave considering $\theta = 0°$ and $kh = 1.00$. In Figure 17, it can be observed that for rectangular-shape, H-shape, Π-shape, and trapezoidal shape HFBs, the total forces and moment is approximately same and periodic in nature having minimum value among all HFBs. But the box-shape HFB shows different behaviour than others shapes of breakwater having the absolute highest value of $F_x = 122$ kN, $F_z = 561$ kN, and $M_y = 1\,126$ kN·m. The variation in F_x (Figure 17(a)) for box-shape HFB is observed to be approximately same as rectangular-shape HFB with some minor increase and decrease over the response time. The F_z (Figure 17(b)) and M_y (Figure 17(c)) for box-shape HFB shows high values (with maximum value of $F_z = 561$ kN and $M_y = 1\,126$ kN·m) up to 60 s and thereafter the values decreased by about 30% (Figure 17(b), (c)).

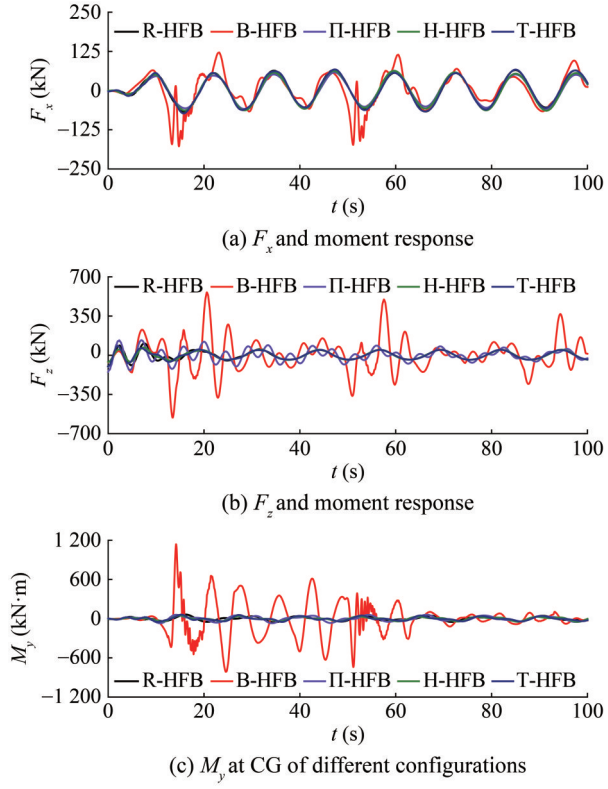

(a) F_x and moment response

(b) F_z and moment response

(c) M_y at CG of different configurations

Figure 17 Total force response of HFBs for $kh = 1.00$ in OM considering $d/h = 0.1$, $b/h = 0.3$ and $\theta = 0°$

In the time series response for box-HFB, the amplitude of forces appears to be irregular when compared to the forces of other HFBs, which could be due to hydrodynamic nonlinearities generated by the high mooring force ($F_{T\max} = 348$ kN for $kh = 1.00$) influencing its dynamic response and interactions. The variation in forces with respect to different HFB models may be due to change in wave interaction characteristics with change in cross sectional shapes.

In the case of CM configuration for $kh = 1.00$ (Figure 18), similar trend as in OM configuration as the F_x for all shapes of HFBs in CM is approximately same for all HFBs (around $F_x = 65$ to 71 kN) except box-HFB ($F_x = 135$ kN) (Figure 18(a)). In Figure 18(b) it can be observed that the total force in z-direction for rectangular, trapezoidal, H and Π-shape HFBs is $F_z = 101, 73, 68, 140$ kN respectively and are periodic in nature. The value of F_z for Box-shape HFB in CM is having similar trend as for OM and maximum force is around $F_z = 583$ kN.

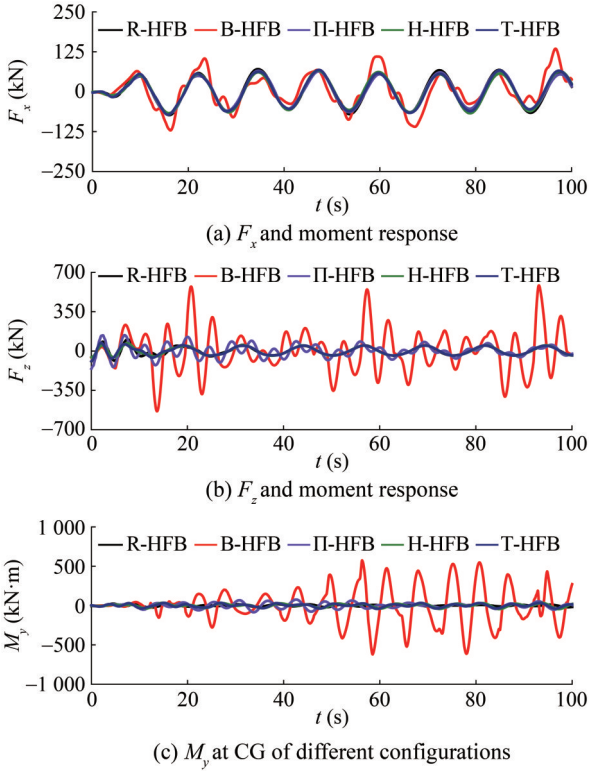

(a) F_x and moment response

(b) F_z and moment response

(c) M_y at CG of different configurations

Figure 18 Total force response of HFBs for $kh = 1.00$ in CM considering $d/h = 0.1$, $b/h = 0.3$ and $\theta = 0°$

The moment response (Figure 18(c)) for box-shape HFB shows high values for longer duration of incident wave and have maximum absolute value of about 575 kN·m. This might be caused due to the nonlinear behaviour of the mooring line or nonlinear interactions between the structure and the surrounding fluid, which can lead to an increase in structural forces with the increase in time. These effects may become more apparent as the simulation progresses, altering the reaction of system and potentially raising stresses. From Figure 17 and Figure 18, it is noted that the total structural moment M_y experienced by HFBs in CM is significantly (about 30% to 65%) less than OM. However, the total structural forces (F_x and F_z) observed to be about 1% to 10% higher in CM over OM for all HFBs. The higher value of forces in CM could be related to balanced loading along the mooring line, and the reduced moment in CM

might be due to the stable nature of the arrangement.

In Figure 19 and Figure 20, the structural force and moment response for short waves in deep water regions (kh > 3.14) for regular wave of wave frequency corresponding to kh = 4.18 for different HFBs in both mooring configurations are presented. It is worth noting that for all HFB models the value of F_x varies in similar manner upto 70 s, which could be due to similar mass of the floating bodies, and further, the value of F_x limited within ±160 kN <F_x < ±260 kN (Figure 19(a)) in case of OM. The vertical force at CG F_z (Figure 19(b)) for rectangular-shape HFB is observed to be having amplitude of 477 kN. Considering rectangular-shape HFB as a base, as rectangular-shape HFB is widely studied shape of floating breakwater, the F_z value in box-shape HFB shows increase of about 64%, Π-shape HFB shows about 18% increment, H-shape HFB shows about 13% decrease, and for trapezoidal-shape HFB F_z is observed to decrease by about 31%. These changes could be attributed to differences in center of buoyancy compared to rectangular-shape HFB. The box and Π-shape HFBs have a lower centre of buoyancy than rectangular-shape HFB, whereas H and trapezoidal-shape HFB have a higher center of buoyancy than rectangular-shape HFB. The lower centre of buoyancy results in a decrease in the stability of floating structures, causing an increase in the forces experienced by the structures. In Figure 19(a), (b), both horizontal and vertical force at CG for trapezoidal-shape HFB is least among all HFB models which might be due to the sloped sea-side facing for the floating breakwater structure. The short waves interact more with floating structures as lot of energy is concentrated near the free surface in deep water regions, but due to sloped face towards incident wave, more waves flow past the structure than vertical facing structure leading to less structural forces. The moment M_y (Figure 19(c)) for rectangular HFB is least among all for OM and M_y varies within −216 kN·m ⩽ M_y ⩽ 236 kN·m over analysed time response. The reason for less moment experienced by structure in case of rectangular-shape HFB may be the large restoring moment being provided by the uniformity of the mass distribution for the rectangular shape. The moment experience by the HFBs of box-shape, H-shape, and trapezoidal-shape in OM case are within −230 kN·m ⩽ M_y ⩽ 305 kN·m, −1 127 kN·m ⩽ M_y ⩽ 1 180 kN·m, and −1 411 kN·m ⩽ M_y ⩽ 1 635 kN·m respectively and are periodic in nature. The highest moment in OM is experience by the Π-shape HFB having maximum absolute value of about 5 159 kN·m. The primary reason behind this large moment is the legs of Π-shape, as most of the mass is concentrated towards the extreme left and right side of the structure aiding the moment at CG. Apart from these observation, one worth noting point is that in comparison to time response of total forces and moment under action of long waves (kh = 1.00), the same response in case of short waves (kh = 4.18) show uniform variation over time.

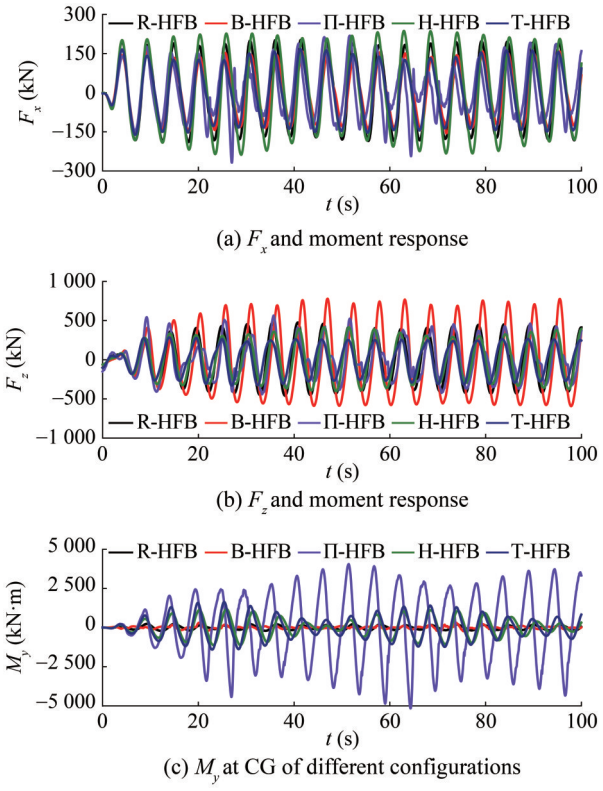

(a) F_x and moment response

(b) F_z and moment response

(c) M_y at CG of different configurations

Figure 19 Total force response of HFBs for kh = 4.18 in OM considering d/h = 0.1, b/h = 0.3 and θ = 0°

In Figure 20, the variation in F_x, F_z, and M_y, in CM configuration for all shapes of HFBs are similar to the case of OM. There is almost minimal difference in forces and small decrease of about 1% in moment is observed in CM with respect to OM of rectangular-shape HFB for kh = 4.18 (Figures 19 and 20). In the case of the box-shape HFB, when compared to OM, 3% increase in F_x, no change in F_z, and 52% decrease in M_y is observed in CM. For Π-shape HFB in CM, F_x is about 12% less, F_z is about 6% more and M_y is about 22% less than the OM respectively. The reduction in moment in case of CM for rectangular, box and Π shape HFBs may be due to greater restoring force provided by the mooring configuration. In the case of the H-shape HFB, the variation is only observed in M_y with an increase of approximately 31%. As for trapezoidal-shape HFB, apart from no change in F_x, the value of F_z and M_y increases by about 5% and 43% respectively for CM in comparison to OM. The increase in M_y in H and trapezoidal-HFB may be due to lack of CM configuration in resisting moment by mooring lines for short waves.

4.5 Transmission coefficient

The transmission coefficient of various HFBs of the

present study is evaluated by analysis of diffraction patterns of each of the structure at a distance of $\lambda/2$ towards the lee-side of the floating structure (Figure 21). Among all HFBs, Π-shape HFB shows transmission coefficient almost equal to 1.00 between $3.14 < kh \leqslant 5.20$, which clearly indicates its unusability as a breakwater as it transmits all incoming waves towards the lee side in the wave frequency range of $3.14 < kh \leqslant 5.20$. However, Π-shape HFB seems to be performing well under the action of very short waves having $kh > 5.20$.

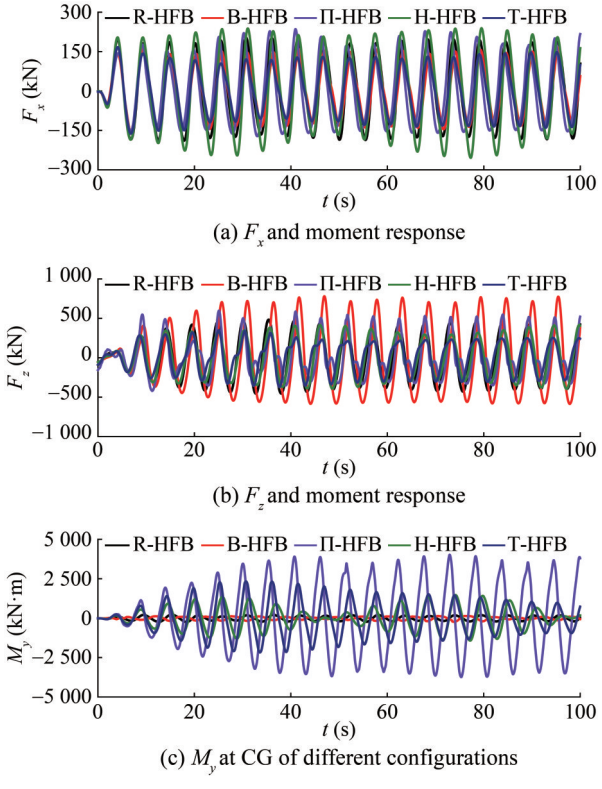

(a) F_x and moment response

(b) F_z and moment response

(c) M_y at CG of different configurations

Figure 20 Total force response of HFBs for $kh = 4.18$ in CM considering $d/h = 0.1$, $b/h = 0.3$ and $\theta = 0°$

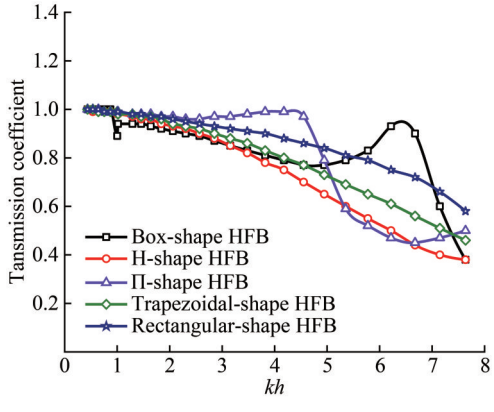

Figure 21 Transmission coefficient versus kh for different HFBs considering $d/h = 0.1$, $b/h = 0.3$, and $\theta = 0°$

In the intermediate and shallow water regions ($kh \leqslant 3.14$), all HFBs have transmission coefficients greater than 0.87, which means the HFBs performed poorly in the said region. But in the deep-water region ($kh > 3.14$), comparing all other types of HFBs with the rectangular-shape HFB, it is worth noting that H and trapezoidal-shape HFBs show less wave transmission than rectangular-HFB, which can be due to better wave attenuation or reflection resulting from changes in the shapes of HFBs. The major reduction in wave transmission coefficient in comparison to rectangular-HFB is found to be in the range of about 13% to 39% in the case of H-shape and about 7% to 23% in the case of trapezoidal-shape in the deep-water region ($kh > 3.14$). The transmission coefficient for box-shape HFB rises for $kh \geqslant 4.95$ and reaches a value of 0.93 at $kh = 6.22$ and again starts dropping. The random behaviour of increase and decrease in wave transmission can be due to the trapping of waves into the hollow portion of box-shape HFB. Further, among all the considered HFBs in deep water regions, the H-shaped HFB performs better in terms of wave attenuation. The enhanced performance is attributed to its larger water plane area among all other HFBs, which intensifies the interaction between waves and structure and facilitates more effective wave energy dissipation by the structure.

5 Conclusions

The present study analyses the performance of mooring line of five different cross-sectional shapes of HFBs and the responses of the HFBs in moored condition. The study is performed based on potential flow theory using Ansys-AQWA to investigate the hydrodynamic performance of the hybrid floating models in case of regular incident wave. The mooring lines are attached with breakwater in OM and CM configurations to examine the mooring line performance in different arrangements for slacked (about 6% to 8% slacked) non-linear catenary mooring lines. To understand the effect of wave incidence, time response analysis is performed to get the maximum mooring line tension $F_{T\max}$ and total structural forces and moment of HFBs. The conclusions drawn from the study are as follows.

1) The comparison of mooring configurations indicates that the cross-mooring configuration results in lower mooring tension for the investigated parameters of the non-linear catenary mooring lines attached with the various forms of HFB models, considering all four mooring lines. The drop in mooring line tension from open mooring to cross mooring is reported to be variable for each type of HFB, however it typically ranges between 20% and 60% for the considered range of wave frequencies.

2) Among all HFB models, the mooring lines of the trapezoidal-shape HFB seems to be experiencing about 17% to 90% lower mooring tension in cross mooring for sea side

cable. The reason for which could be the less movement of structure under regular wave action due to the inclined face towards the wave incidence side. This can cause hydrodynamic forces to operate indirectly rather than directly on the floating structure, leading to a reduced motion response for the trapezoidal-shaped HFB.

3) For box, Π, and H-shape HFBs under action of regular waves of $0.87 \leqslant kh \leqslant 1.00$, $4.55 \leqslant kh \leqslant 4.95$, and $3.15 \leqslant kh \leqslant 3.82$ respectively, the mooring line tension in the seaside cable in the open mooring case is found to exceed the maximum expected tension by about 1.3 to 1.9 times. This may result in the mooring line snapping or breaking.

4) Based on frequency domain analysis, the RAO response in surge and heave is found to be unaffected by connection of mooring lines due to slacked mooring and similar observation is noted for floating rectangular pontoon (Sannasiraj et al., 1998). However, due to the high connection stiffness provided to the HFBs by the mooring lines in rotational directions restricts the pitching motion of the HFBs, showing decrease of about 70% to 99% in pitch RAO for moored case.

5) Based on time response analysis for two distinct wave frequencies for long gravity wave and short gravity wave, the structural forces and moment are determined. It is found that box-shape HFB experiences highest value of structural forces and moment among different shapes of HFBs in both mooring configurations for long waves. In case of short waves horizontal force is highest for Π-shape HFB in OM and for H-shape HFB in CM and lowest for box-shape HFB among all HFBs in both mooring configurations, but the vertical force is highest for box-shape and lowest for trapezoidal shape in both mooring cases, and the moment is highest for Π-shape HFB in both mooring cases and lowest for box-HFB in CM and rectangular-HFB in OM.

6) The transmission coefficient for different shapes of HFBs is investigated considering the diffraction theory for the floating structures, and it is worth noting that trapezoidal and H-shape HFBs provide better wave attenuation than rectangular-shape HFB for deep water regions. The transmission coefficient for H-shape HFB observed to be below 0.75 for most of the deep-water regions.

The present study performed are based on geometric parameters considering $d/h = 0.1$, $b/h = 0.3$, and $\theta = 0°$, which are fixed to better understand the effect of other variations such as the shape of the floating structure and the mooring configurations. The study suggest that the shape and mooring configuration changes have a substantial impact on the forces acting on the structure, motions, wave attenuation characteristics, and tensile forces experienced by the mooring lines. The present investigation explores at the impacts of mooring on different shapes of hybrid floating breakwaters, using open and cross mooring configurations to assess the effects of the configuration and noted that the cross-mooring configuration can be used to reduce mooring line tension. Although there will be friction upon installation of cross moorings, this may be investigated further through experimental studies, and friction reduction techniques can also be explored. The mooring lines of trapezoidal-shape HFB were found to be experiencing the least tension to stabilize the HFB; this finding suggests a low cost of mooring, and further study on improving wave energy conversion from trapezoidal-HFB can be economical. The total structural forces and moments helps in designing the HFB structures with respect to the shape of the hybrid floating body for their better performance in terms of wave attenuation, structural integrity, and stability. Therefore, the hybrid floating structure can be further optimized for most effective and efficient performance in terms of its hydrodynamic characteristics through proper tuning of mooring configurations and structural parameters.

Nomenclature

a_{wave}	Incident wave amplitude
$\boldsymbol{a}$	Fluid particle acceleration
$\boldsymbol{a}_j$	Acceleration of cable at jth node
A_j	Axial directional tensor
A_{ji}	Added mass coefficient
$\boldsymbol{A}_\omega$, $\boldsymbol{A}_\infty$	Added mass matrix at wave frequency and infinite frequency respectively
AE	Cable stiffness per unit length
b	Width of hybrid floating breakwater
B_{ji}	Wave radiation damping coefficient
$\boldsymbol{B}_\omega$	Damping matrix at wave frequency
$\boldsymbol{c}$	Total damping matrix
c_i	Inlet chamber height of OWC
c_o	Air flow outlet diameter of OWC
c_x	Chamber width of OWC
C_d, C_x	Transverse and inline drag coefficients
d	Draft of hybrid floating breakwater
D_j	Unstretched elemental diameter
$F_{a,\,j}$	Wave excitation force in jth direction
$F_{D,\,j}$	Diffraction force in jth direction
$F_{\text{FK},\,j}$	Froude-Krylov force in jth direction
F_b	Buoyant force on mooring cable
F_d	Drag force on mooring cable
F_h	Hydrodynamic force on mooring cable
$F_{r,\,ji}$	Radiation force due to ith motion in jth direction of structure
$F_{T\max}$	Maximum tension experience by mooring line
F_x, F_z	Total force at centre of gravity of structure in respective direction
g	Acceleration due to gravity
h	Depth of seabed from free water surface
$\boldsymbol{h}'(t)$	Acceleration impulse function matrix
H_1, H_2	Horizontal force components of respective tensile force

k	Wave number
$\boldsymbol{K}$	Total stiffness matrix of the floating structure
$\boldsymbol{K}_g$	Complete stiffness matrix of each mooring line
L	Length of hybrid floating breakwater
L_j	Unstretched elemental length
L_{us}	Unstretched length of mooring line
$\boldsymbol{m}$	Mass matrix of floating structure
m_a	Added mass
M	Catenary profile originating point for mooring cable
M_1, M_2	Starting and end point coordinates of a cable segment
M_y	Total moment at the centre of gravity of structure
N_j	Normal directional tensor
$\hat{n}_j$	Generalised surface normal for *j*th direction
$p_t(t)$	Hydrodynamic pressure
$\boldsymbol{P}_m$	Matrix of mooring line tension at attachment points
$\boldsymbol{R}_a$	Matrix of coordinates of mooring attachment points on structure
$\boldsymbol{R}(t)$	Velocity impulse function matrix
S	Wetted surface of the floating structure
S'	Unstretched length of cable segment
T_1, T_2	Tensile force at the starting and end point of a cable segment.
$\boldsymbol{U}_j(t)$	Matrix form of the current velocity *j*th node at time *t*
$\vec{V}$	Fluid particle velocity
V_1, V_2	Vertical force components of respective tensile force
$\boldsymbol{V}_j(t)$	Matrix form of the structural velocity *j*th node at time *t*
x_j	*j*th motion per unit wave amplitude
α	Wave phase
ζ	Free surface elevation
θ	Wave incidence angle
λ	Wave length
ρ	Density of fluid i.e., sea water
φ_I	Incident velocity potential
φ_D	Diffracted velocity potential
φ_R	Radiated velocity potential
$\varphi_{R,i}^{\mathrm{Img}}, \varphi_{R,i}^{\mathrm{Re}}$	Imaginary and real part of radiated velocity potential
ω	Wave frequency

Competing interest Debabrata Karmakar is an editorial board member for the Journal of Marine Science and Application and was not involved in the editorial review, or the decision to publish this article. All authors declare that there are no other competing interests.

References

ANSYS (2021) ANSYS AQWA Theory Manual, ANSYS Inc., Canonsburg, PA, USA

Barltrop N (1998) Floating structures: a guide for design and analysis. CMPT

Cheng X, Li S, Wang G (2023) Experimental study on hydrodynamic characteristics of barge-type breakwaters under different mooring methods. Journal of Marine Science and Engineering 11(5): 1016

Dai J, Wang CM, Utsunomiya T, Duan W (2018) Review of recent research and developments on floating breakwaters. Ocean Engineering 158: 132-151

Depalo F, Wang S, Xu S, Guedes Soares C (2021) Design and analysis of a mooring system for a wave energy converter. Journal of Marine Science and Engineering 9(7): 782

Diamantoulaki I, Angelides DC (2011) Modeling of cable-moored floating breakwaters connected with hinges. Engineering Structures 33(5): 1536-1552

Dong GH, Zheng YN, Li YC, Teng B, Guan CT, Lin DF (2008) Experiments on wave transmission coefficients of floating breakwaters. Ocean Engineering 35(8-9): 931-938

Elchahal G, Younes R, Lafon P (2009) Parametrical and motion analysis of a moored rectangular floating breakwater. Journal of Offshore Mechanics and Arctic Engineering 131(3)

Ji CY, Chen X, Cui J, Yuan ZM, Incecik A (2015) Experimental study of a new type of floating breakwater. Ocean Engineering 105: 295-303

Lee J, Cho W (2003) Hydrodynamic analysis of wave interactions with a moored floating breakwater using the element-free Galerkin method. Canadian Journal of Civil Engineering 30(4): 720-733

Li CB, Chen M, Choung J (2021) The quasi-static response of moored floating structures based on minimization of mechanical energy. Journal of Marine Science and Engineering 9(9): 960

Liang JM, Liu Y, Chen YK, Li AJ (2022) Experimental study on hydrodynamic characteristics of the box-type floating breakwater with different mooring configurations. Ocean Engineering 254: 111296

Liu Z, Wang Y (2020) Numerical studies of submerged moored box-type floating breakwaters with different shapes of cross-sections using SPH. Coastal Engineering 158: 103687

Loukogeorgaki E, Angelides DC (2005) Stiffness of mooring lines and performance of floating breakwater in three dimensions. Applied Ocean Research 27(4-5): 187-208

Loukogeorgaki E, Yagci O, Kabdasli MS (2014) 3D Experimental investigation of the structural response and the effectiveness of a moored floating breakwater with flexibly connected modules. Coastal Engineering 91: 164-180

Mustapa MA, Yaakob OB, Ahmed YM, Rheem CK, Koh KK, Adnan FA (2017) Wave energy device and breakwater integration: A review. Renewable and Sustainable Energy Reviews 77: 43-58

Nikpour AH, Moghim MN, Badri MA (2019) Experimental study of wave attenuation in trapezoidal floating breakwaters. China Ocean Engineering 33: 103-113

Pols A, Gubesch E, Abdussamie N, Penesis I, Chin C (2021) Mooring analysis of a floating OWC wave energy converter. Journal of Marine Science and Engineering 9(2): 228

Rajabi M, Ghassemi H (2021) Hydrodynamic performance improvement of double-row floating breakwaters by changing the cross-sectional geometry. Mathematical Problems in Engineering 2021: 1-21

Sannasiraj SA, Sundar V, Sundaravadivelu R (1998) Mooring forces and motion responses of pontoon-type floating breakwaters. Ocean Engineering 25(1): 27-48

Wang CM, Tay ZY (2011) Very large floating structures: applications, research and development. Procedia Engineering 14: 62-72

Williams AN, Abul-Azm AG (1997) Dual pontoon floating breakwater.

Ocean Engineering 24(5): 465-478
Williams AN, Lee HS, Huang Z (2000) Floating pontoon breakwaters. Ocean Engineering 27(3): 221-240
Xu S, Wang S, Guedes Soares C (2019) Review of mooring design for floating wave energy converters. Renewable and Sustainable Energy Reviews 111: 595-621
Yamamoto T (1981) Moored floating breakwater response to regular and irregular waves. Applied Ocean Research 3(1): 27-36
Yamamoto T, Yoshida A, Ijima T (1980) Dynamics of elastically moored floating objects. Applied Ocean Research 2(2): 85-92
Yoon JS, Ha T, Jung J (2018) Laboratory experiments on characteristics of perforated-type floating breakwaters. Journal of Coastal Research 85(10085): 1051-1055
Yuan ZM, Incecik A, Ji C (2014) Numerical study on a hybrid mooring system with clump weights and buoys. Ocean Engineering 88: 1-11
Zanden JVD, Hout AJVD, Otto W, Spaargaren F, Walles B, Wilde JD (2022) Experimental study on a breaking-enforcing floating breakwater. Journal of Coastal and Hydraulic Structures 2: 18
Zang Z, Fang Z, Qiao K, Zhao L, Zhou T (2024) Numerical study on wave dissipation and mooring force of a horizontal multi-cylinder floating breakwater. Journal of Marine Science and Engineering 12(3): 449
Zhang A, Li S, Cui P, Li S, Liu Y (2023) A unified theory for bubble dynamics. Physics of Fluids 35: 033323
Zhang D, Zhao B, Jiang H (2024) Wave energy converter with floating-point absorber and catenary mooring: dynamic coupling analysis. Frontiers in Marine Science 11: 1338330
Zhao C, Stansby P, Johanning L (2023) OrcaFlex predictions for a multi-float hinged WEC with nonlinear mooring systems: Elastic mooring force and dynamic motion. Ocean Engineering 286: 115504
Zhao XL, Ning DZ, Zou QP, Qiao DS, Cai SQ (2019) Hybrid floating breakwater-WEC system: A review. Ocean Engineering 186: 106126